JOURNAL OF GEOPHYSICAL RESEARCH, VOL. 86, NO. C6, PAGES 5325-5338, JUNE 20, 1981

Ozone in the Upper Stratosphere and Mesosphere

MICHAEL J. PRATHER

Center for Earth and Planetary Physics, Harvard University, Cambridge, Massachusetts 02138

A detailed photochemical model of the upper stratosphere and mesosphere is compared with three extensive sets of ozone observations: Atmospheric Explorer-E backscattered ultraviolet experiment (BUV), Nimbus-4 BUV, and rocket flights from Wallops Flight Center (ROCOZ). The Nimbus-4 and rocket observations are most sensitive to ozone between 30 and 50 km, whereas observations from AE-E measure the abundance of ozone up to 70 km. The photochemical model accurately reproduces the observed relationship between BUV intensity and local solar zenith angle, although the absolute calibration on AE-E appears to be in error. The AE-E observations and the model both exhibit a morning-afternoon asymmetry, with more ozone in the morning owing to the build up of HO_x species in the afternoon. Seasonal changes in atmospheric temperature produce an annual maximum in tropical mesospheric ozone during June-July-August. The amplitude of the observed effect is somewhat larger than calculated by the model. Some problems appear to remain with the presently accepted kinetic rates for HO_x species in the atmosphere.

1. INTRODUCTION

Absorption of ultraviolet sunlight by ozone and molecular oxygen provides the energy which maintains the temperature structure and wind field of the middle atmosphere [*Murgatroyd and Singleton,* 1961; *Leovy,* 1964]. The daily heating is maximal near the stratopause and induces diurnal and semidiurnal tides which are important to the structure and vertical transports of the upper mesosphere and thermosphere [*Lindzen,* 1979; *Forbes and Garrett,* 1979]. Thus the distribution of ozone plays a major role in determining the mean circulation of the upper atmosphere.

The concentration of ozone in the upper stratosphere and lower mesosphere is controlled by photochemical production and loss. Radicals containing hydrogen (OH, HO_2, H), chlorine (Cl, ClO), and nitrogen (NO, NO_2, NO_3) all play important roles through reactions with each other, with ozone and with atomic oxygen [*Chapman,* 1930; *Bates and Nicolet,* 1950; *Hampson,* 1964; *Wofsy and McElroy,* 1974]. As discussed in section 2, these reactions proceed so rapidly that transport of ozone and other radicals plays a minor role in determining the ozone distribution between 35 and 80 km.

The present research focuses on chemical models and observational data in the upper stratosphere and the mesosphere. This region of the atmosphere contains less than 25% of the total ozone but is often assumed to be the photochemical source region for ozone in the lower atmosphere [*Mahlman et al.,* 1980]. The complex and poorly characterized molecules which are of interest in the lower stratosphere (e.g., HOCl, $ClNO_3$, $HOONO_2$, N_2O_5 [*National Academy of Sciences,* 1979]) are not important in the photochemistry above 35 km, where three-body reactions proceed slowly and the ultraviolet radiation field is relatively more intense.

This paper examines three recently available sets of observations of ozone in the stratosphere and mesosphere. Each data set is comprised of many individual observations acquired over periods longer than a year. Two of these data sets (Atmospheric Explorer-E and Nimbus-4) are based on satellite monitoring of backscattered ultraviolet sunlight (BUV). The third set consists of rocket measurements of ozone from the differential absorption of sunlight as a function of altitude (rocket ozone project (ROCOZ) [*Krueger and Wright,* 1979]). A primary question which must be answered is whether these three data sets provide a consistent picture of ozone in the upper stratosphere and mesosphere.

The analysis of the complete set of data from Atmospheric Explorer-E (BUV) and a limited set of Nimbus-4 data [*Heath et al.,* 1979] is presented in section 3, where differences between the two data sets are discussed with attention to seasonal variations. Results from the theoretical model are compared in turn with the ozone concentrations of the mid-latitude ROCOZ data and with the satellite albedos from the tropics.

A major goal of this research is the development of an objective photochemical model which, as accurately as possible, reproduces all aspects of the observed distribution of ozone. In section 4 the overall validity of this photochemical model is critically examined. The key uncertainties in the model are pointed out, and weaknesses or inconsistencies among the observational data for ozone are discussed.

2. PHOTOCHEMICAL MODEL

The photochemistry which controls the abundance of ozone in the upper stratosphere and mesosphere can be described by about 50 kinetic and photolytic reactions as given in Table 1. The definitions of odd-oxygen ($O_x = O_3 + O + NO_2 + ClO$) and odd-hydrogen ($HO_x = H + OH + HO_2$) encompass those species which rapidly interchange with one another. These are displayed schematically in Figure 1. The photochemical lifetime for each family ranges from hours to days and is shown in Figure 2.

a. Chemistry

The rates of chemical reactions which produce or destroy odd-oxygen are given in Figure 3. The only significant source of odd-oxygen above 30 km is the photolysis of molecular oxygen [*Chapman,* 1930].

(R38) $$O_2 + h\nu \rightarrow O + O$$

The dominant sinks for O_x in the mesosphere (45–80 km) are the reactions of atomic oxygen with members of the HO_x family [*Bates and Nicolet,* 1950].

(R4) $$O + OH \rightarrow H + O_2$$

(R5) $$O + HO_2 \rightarrow OH + O_2$$

Paper number 80C1473.
0148-0227/81/080C-1473$01.00

TABLE 1. Photochemical Reactions

	Reactions	Rate ($cm^3\ s^{-1}$ or $cm^6\ s^{-1}$)		Note*
(R1)	$O + O_2 + M = O_3 + M$	1.05E-34	$\exp(+510/T)$	LPWM
(R2)	$O + O_3 = O_2 + O_2$	1.5E-11	$\exp(-2218/T)$	NASA
(R3)	$O + O + M = O_2 + M$	9.6E-34	$\exp(+480/T)$	LPWM
(R4)	$O + OH = H + O_2$	4.0E-11		NASA
(R5)	$O + HO_2 = OH + O_2$	3.5E-11		NASA
(R6)	$O + H_2 = OH + H$	5.3E-11	$\exp(-5100/T)$	LPWM
(R7)	$O(^1D) + N_2 = O + N_2$	2.0E-11	$\exp(+107/T)$	NASA
(R8)	$O(^1D) + O_2 = O + O_2$	2.9E-11	$\exp(+67/T)$	NASA
(R9)	$O(^1D) + H_2O = OH + OH$	2.3E-10		NASA
(R10)	$O(^1D) + H_2 = OH + H$	0.99E-10		NASA
(R11)	$O_3 + H = OH + O_2$	1.4E-10	$\exp(-470/T)$	NASA
(R12)	$O_3 + OH = HO_2 + O_2$	1.6E-12	$\exp(-940/T)$	NASA
(R13)	$O_3 + HO_2 = OH + O_2 + O_2$	1.1E-14	$\exp(-580/T)$	NASA
(R14)	$H + O_2 + M = HO_2 + M$	1.90E-32	$\exp(+350/T)$	LPWM
(R15)	$H + HO_2 = H_2 + O_2$	4.2E-11	$\exp(-350/T)$	LPWM
(R16)	$H + HO_2 = OH + OH$	4.2E-10	$\exp(-950/T)$	LPWM
(R17)	$OH + HO_2 = H_2O + O_2$	4.0E-11		NASA
(R18)	$OH + H_2 = H_2O + H$	1.2E-11	$\exp(-2200/T)$	NASA
(R19)	$OH + CO = CO_2 + H$	1.35E-13	[1 + p(atm)]	NASA
(R20)	$OH + OH = H_2O + O$	1.0E-11	$\exp(-500/T)$	NASA
(R21)	$NO + O + M = NO_2 + M$	4.0E-33	$\exp(+940/T)$	LPWM
(R22)	$NO + HO_2 = NO_2 + OH$	3.4E-12	$\exp(+250/T)$	NASA
(R23)	$NO + O_3 = NO_2 + O_2$	2.3E-12	$\exp(-1450/T)$	NASA
(R24)	$NO_2 + O = NO + O_2$	9.3E-12		NASA
(R25)	$NO_2 + H = NO + OH$	4.8E-10	$\exp(-405/T)$	NASA
(R26)	$N + NO = N_2 + O$	3.4E-11		NASA
(R27)	$N + O_2 = NO + O$	4.4E-12	$\exp(-3220/T)$	NASA
(R28)	$HCl + OH = Cl + H_2O$	2.8E-12	$\exp(-425/T)$	NASA
(R29)	$HCl + H = Cl + H_2$	2.3E-11	$\exp(-1816/T)$	LPWM
(R30)	$Cl + H_2 = HCl + H$	3.5E-11	$\exp(-2290/T)$	NASA
(R31)	$Cl + CH_4 = HCl + CH_3$	9.9E-12	$\exp(-1359/T)$	NASA
(R32)	$Cl + HO_2 = HCl + O_2$	4.5E-11		NASA
(R33)	$Cl + O_3 = ClO + O_2$	2.8E-11	$\exp(-257/T)$	NASA
(R34)	$ClO + NO = Cl + NO_2$	7.8E-12	$\exp(+250/T)$	NASA
(R35)	$ClO + O = Cl + O_2$	7.7E-11	$\exp(-130/T)$	NASA
(R36)	$CH_4 + OH = H_2O + CH_3$	2.4E-12	$\exp(-1710/T)$	NASA
(R37)	$CH_4 + O(^1D) = OH + CH_3$	1.4E-10		NASA
(R38)	$O_2 + h\nu = O + O$			
(R39)	$O_3 + h\nu = O_2(^1\Delta) + O(^1D)$			
(R40)	$O_3 + h\nu = O_2 + O$			
(R41)	$HO_2 + h\nu = OH + O$			
(R42)	$H_2O + h\nu = OH + H$			
(R43)	$NO_2 + h\nu = NO + O$			
(R44)	$NO + h\nu = N + O$			
(R45)	$HCl + h\nu = H + Cl$			
(R46)	$ClO + h\nu = Cl + O$			
(R47)	$CH_4 + h\nu = H_2 + CH_2$			

*NASA refers to *NASA-JPL* [1979]. LPWM refers to Logan *et al.* [1978].

In the upper stratosphere (30–45 km), the major losses of odd-oxygen are due to NO_x catalytic cycles [*Hampson,* 1964],

(R23) $NO + O_3 \rightarrow NO_2 + O_2$

(R24) $NO_2 + O \rightarrow NO + O_2$

to Cl_x catalytic cycles [*Stolarski and Cicerone,* 1974; *Wofsy and McElroy,* 1974],

(R33) $Cl + O_3 \rightarrow ClO + O_2$

(R35) $ClO + O \rightarrow Cl + O_2$

and to the self-reaction [*Chapman,* 1930],

(R2) $O + O_3 \rightarrow O_2 + O_2$

The reaction rate constant k for all of the above reactions are taken from the recent *NASA-JPL* [1979] review. The largest uncertainties (±50%) are associated with k_4 and k_5. The photolysis rate for molecular oxygen is calculated from the solar flux and cross-section data in Table 2 and from the treatment of the Schumann-Runge bands described in *Logan et al.* [1978]. The resulting O_2 dissociation rates are similar (±10%) to those of *Frederick and Hudson* [1980].

The odd-oxygen budget of the mesosphere is strongly

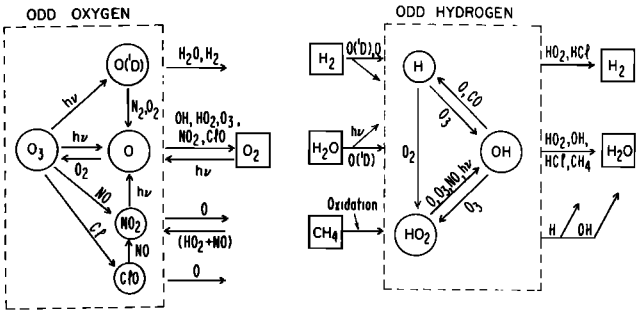

Fig. 1. Photochemical reactions for the mesosphere and the upper stratosphere.

coupled to the chemistry of odd-hydrogen [*Bates and Nicolet*, 1950; *Hunt*, 1966; *Liu and Donahue*, 1974]. Figure 4 presents the rates of specific reactions which control concentrations of HO_x species. Production of odd-hydrogen is dominated by

(R9) $$O(^1D) + H_2O \rightarrow OH + OH$$

below 60 km and by

(R42) $$H_2O + h\nu \rightarrow H + OH$$

above 65 km. Below 70 km, over 90% of the HO_x loss is due to

(R17) $$OH + HO_2 \rightarrow H_2O + O_2$$

Above 70 km, significant HO_x loss occurs through

(R15) $$H + HO_2 \rightarrow H_2 + O_2$$

The rates for the HO_x production reactions are reasonably well determined [*Baulch et al.*, 1980; *NASA-JPL*, 1979], but the reaction rates k_{17} and k_{15} remain uncertain. The *NASA-JPL* [1979] value for (R17), $k_{17} = 4.0 \times 10^{-11}$ cm^3 s^{-1}, is based on low pressure measurements [*Burrows et al.*, 1977; *Chang and Kaufman*, 1978] and is much smaller than the values at atmospheric pressure reported by *DeMore* [1979], $k_{17} \geq 1 \times 10^{-10}$ cm^3 s^{-1}. The measurements made at a pressure of 2–4 torr employed inert carrier gases with at most traces of molecular oxygen. If we accept DeMore's hypothesis of a pressure-dependent reaction rate, then the present kinetic data do not determine rates applicable in the atmosphere.

Because (R17) is the dominant path for odd-hydrogen recombination below 75 km, a change in k_{17} has the same effect on model calculations as a change of opposite sign in H_2O, the primary source for odd-hydrogen. In particular, the standard kinetic model with $k_{17} = 4 \times 10^{-11}$ cm^3 s^{-1} and 2 ppm H_2O would produce the same HO_x distributions below 75 km as a model with DeMore's rate $k_{17} = 1 \times 10^{-10}$ cm^3 s^{-1} and 5 ppm H_2O.

The rate constant for (R15) has been measured only at room temperature [*Hack et al.*, 1978, 1979], and thus the temperature dependence adopted here [*Baulch et al.*, 1972] is not well determined. This reaction (R15) is most important to the HO_x budget near the extremely cold mesopause (~190°K). If this reaction has no temperature dependence, then it proceeds twice as fast at the mesopause as compared to the expression in Table 1. The concentrations of HO_x are reduced accordingly, and the O_x abundance should increase near the mesopause.

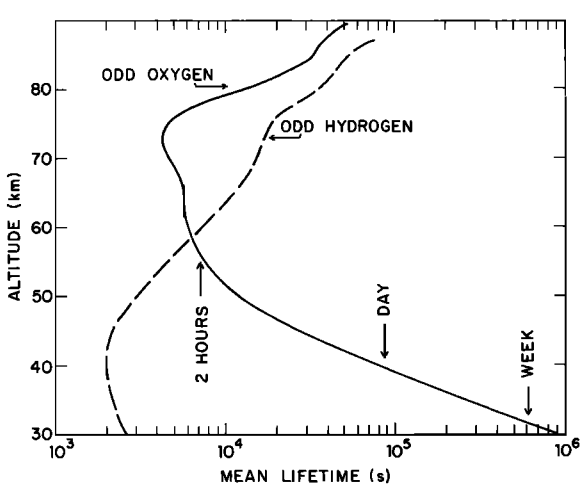

Fig. 2. Mean photochemical lifetime of odd-oxygen and odd-hydrogen as a function of altitude. The definition of odd-oxygen and odd-hydrogen are shown in Figure 1. The lifetime for the standard photochemical model with the 15°N annual atmosphere is defined as the noontime concentration divided by the production which has been averaged over 24 hours.

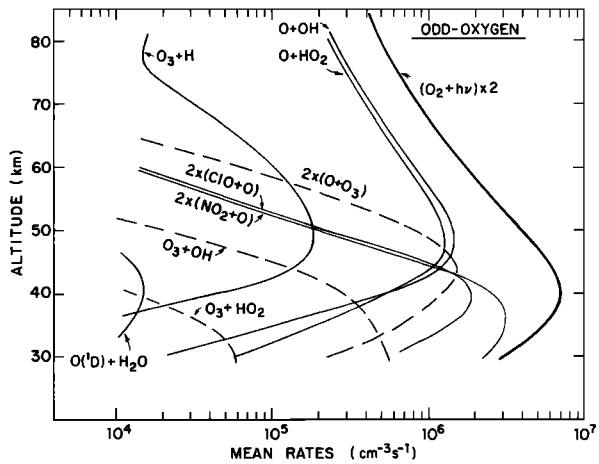

Fig. 3. Vertical profile of mean photochemical rates which are important to odd-oxygen. For the model described in Figure 2, the rates have been averaged over 24 hours.

b. *Time Dependent Calculations*

The diurnal variations of the concentrations of chemical species n_i (cm^{-3}) over the 24-hour day are calculated from the continuity equation,

$$\frac{dn_i}{dt} = P_i - L_i + \nabla \cdot \phi_i \qquad (1)$$

where P_i, L_i and $\nabla \cdot \phi_i$ are the local production, local loss, and divergence of the flux for species i, respectively (cm^{-3} s^{-1}). For short-lived species P and L will be much larger than $\nabla \cdot \phi_i$. Consequently, the calculations presented here assume that transport of radicals is negligible, and the flux divergence term in (1) is neglected for all species.

The local production and loss terms in (1) involve products of concentrations of other chemical species. The coupled set of continuity equations is accordingly nonlinear. The inverse Euler technique is used to solve (implicitly) for species concentrations at each new time step. The mass of any closed system is conserved to 1 part in 10^{10}. Time steps of the order of 1 hour are used to model the 24-hour day with finer temporal resolution near sunrise and sunset. Steady state conditions are achieved by an acceleration procedure which ensures that the net change in concentration of all species is zero after a 24-hour model day [*Wofsy*, 1978].

c. *Solar Radiation and BUV Albedos*

The radiation field is calculated at each time step during the model day for the true zenith angle of the sun. The model includes absorption by molecular oxygen and ozone as well as molecular scattering. The attenuation of the direct solar flux is calculated by integrating through the atmosphere in the direction of the sun. The calculation takes into account both sphericity and changes in local solar time along the path. Refraction is not included. This direct solar flux is the source function used to calculate the diffuse radiation in an inhomogeneous scattering atmosphere which is assumed to be plane parallel [*Prather*, 1974]. The method allows the calcu-

TABLE 2. Solar Flux and Cross Sections

λ, (Å)	Flux*	O_2*	O_3	H_2O	q‡
1215.6	2.51 + 11†	1.0 − 20		1.43 − 17	
1700	2.01 + 11	8.8 − 19		4.2 − 18	
1750	2.94 + 11	2.7 − 19	0.83 − 18	2.7 − 18	
1800	5.32 + 11	SR bands	0.76 − 18	7.5 − 19	
1850	6.90 + 11	SR bands	0.69 − 18	5.0 − 20	
1900	1.09 + 12	SR bands	0.53 − 18	5.2 − 21	
1950	2.40 + 12	SR bands	0.41 − 18	6.3 − 22	
2000	3.75 + 12	SR bands	0.31 − 18	6.3 − 23	
2050	5.71 + 12	1.0 − 23	0.34 − 18		
2100	1.48 + 13	8.5 − 24	0.53 − 18		
2150	2.10 + 13	6.5 − 24	1.02 − 18		
2200	2.59 + 13	5.0 − 24	1.82 − 18		
2250	3.21 + 13	4.0 − 24	2.94 − 18		
2300	3.56 + 13	3.0 − 24	4.51 − 18		
2350	3.66 + 13	1.6 − 24	6.34 − 18		
2400	3.76 + 13	1.0 − 24	8.26 − 18		
2450	3.86 + 13	7.0 − 25	1.00 − 17		
2500	3.97 + 13	3.0 − 25	1.11 − 17		
2550	5.18 + 13	1.2 − 25	1.17 − 17		
2600	8.54 + 13		1.11 − 17		
2650	1.41 + 14		9.86 − 18		
2700	1.59 + 14		7.85 − 18		
2750	1.44 + 14		5.83 − 18		
2800	1.74 + 14		3.99 − 18		
2850	2.33 + 14		2.47 − 18		
2900	3.15 + 14		1.37 − 18		
2950	3.89 + 14		0.76 − 18		1.00
3000	3.85 + 14		0.38 − 18		1.00
3050	4.28 + 14		0.18 − 18		0.95
3100	7.84 + 14		0.99 − 19		0.45
3200	1.32 + 15		0.24 − 19		0.00
3300	1.59 + 15		0.69 − 20		0.00
3400	1.69 + 15		1.71 − 21		0.00
3500	1.80 + 15		0.43 − 22		0.00
3600	2.99 + 15		...		...
3800	4.19 + 15		...		...
4000	2.27 + 16		...		...
5000	4.85 + 16		...		...
6000	7.38 + 16		4.60 − 21		0.00

In squared centimeters.

Sources: Flux, Vernazza et al. [1976], Hinteregger [1979]; O_2, see *Logan et al.* [1978]; O_3, *Griggs* [1968], quantum yield of $O(^1D)$ from *NASA-JPL* [1979]; H_2O, *Watanabe et al.* [1953], *Thompson et al.* [1963]; NO_2, *NASA-JPL* [1979]; CH_4, HCl, ClO, HO_2, see *Logan et al.* [1978].

* Solar flux in units: photons cm^{-2} s^{-1} $interval^{-1}$ at 1 AU. Cross sections in units: cm^2.

† Read 2.51 + 11 as $2.51 \times 10^{+11}$.

‡ Quantum yield of $O(^1D)$ at 260°K.

lation of photolytic rates for solar zenith angles as great as 99°. The solar extinction near twilight requires knowledge of the behavior of ozone at other local solar times. Solutions are iterative and converge to the order of 10^{-3} in approximately four iterations.

The backscattered radiance from the atmosphere may be calculated from the time-dependent distribution of ozone.

$$I = \frac{F_0}{4\pi} \int d\tau \cdot \tilde{\omega}(\tau) \cdot P(\tau, \pi - \theta) \exp[-\tau - \tau_*] \qquad (2)$$

In this case, I is the monochromatic intensity of light scattered in the direction of the zenith, F_0 is the incident solar flux, P is the scattering phase function for natural light, θ is the solar zenith angle, $\tilde{\omega}$ is the single scattering albedo, τ is the vertical extinction, and τ_* is the extinction path in the direction of the sun [see *Chandrasekhar,* 1960]. One may define the dimensionless BUV albedo

$$p_\lambda(\theta) = 4\pi I_\lambda(\theta)/F_{0\lambda} \qquad (3)$$

The incident light is assumed to be unpolarized, and the scattered intensities of different polarization states have been combined. Only first-order scattering is included in (2). Higher-order scattering may be included rigorously [*Prather,* 1974] but was found to be of little importance for wavelengths less than or equal to 2922 Å. In these cases the solar flux does not penetrate significantly below 30 km, and the vertical scattering depth is at most 0.01.

The calculations assume that the only source of scattered light is due to Rayleigh and Raman scattering by the molecules of the background atmosphere (N_2, O_2, CO_2). The mean Rayleigh scattering cross section per molecule is given by [*Penndorf,* 1957]

$$\sigma_{Ray} = \frac{8}{3} \pi^3 \lambda^{-4} (n_s^2 - 1)^2 N_s^{-2} =$$

$$= 5.10 \times 10^{-21} \lambda^{-4} (n_s - 1)^2 \text{ cm}^2 \qquad (4)$$

where λ is the wavelength (μm), N_s is the molecular density at 15°C (cm^{-3}), and n_s is the index of refraction for air at 15°C [*Edlen,* 1953].

$$(n_s - 1) \times 10^6 = 64.328 + 29498.1/(146 - \lambda^{-2}) + 255.4/(41 - \lambda^{-2}) \qquad (5)$$

Rotational Raman scattering will contribute significantly to the measured quantity of scattered light if the incident source is nearly continuous with wavelength or if the source is monochromatic and the instrument cannot resolve the rotational Raman shift of up to 20 Å. The Raman scattered light consists of an unshifted component as well as two wings which are distributed according to the population of rotational states of the scattering gas. For air between 200°K and 300°K the relative intensities of the Stokes ($\Delta J = +2$), central ($\Delta J = 0$), and anti-Stokes ($\Delta J = -2$) components are 0.43, 0.26, and 0.31, respectively. *Penney et al.* [1974] attribute the entire depolarized component of Rayleigh scattered light to rotational Raman scattering. The total cross section for this process is

$$\sigma_{RRS} = 1.39 \times 10^{-29}\lambda^{-4.5} \text{ cm}^2 \quad (6)$$

where the additional factor of −0.5 in the exponent of $\lambda(\mu m)$ is indicated by the wavelength dependence of the anisotropy of the polarizability [*Penney et al.*, 1974]. The cross section for vibrational Raman scattering [*Hyatt et al.*, 1973; *Penney et al.*, 1974] is approximately an order of magnitude smaller than that for rotational Raman and may be ignored in the present context.

For a given wavelength in the interval 2500–3000 Å, rotational Raman scattering contributes an additional 5.9% to the Rayleigh extinction cross section but only an extra 1.5% to the scattered light at the incident wavelength, λ_0. The remaining 4.4% is scattered at a shifted wavelength into wings of width 10 Å on either side of λ_0. If we ignore this shift in wavelength, the cross section and phase function for Rayleigh + Raman scattering by air can be defined as

$$\sigma_m = 5.40 \times 10^{-21}\lambda^{-4}(n_s - 1)^2 \text{ cm}^2 \quad (7)$$

$$P_m(x) = 0.7625 + 0.7124 \cos^2 x \quad (8)$$

where x is the scattering angle. These expressions are similar to *Penndorf*'s [1957] formulation with a depolarization of $\rho = 0.035$. The error induced in the 2500–3000 Å albedos by neglecting the finite bandwidth of the scattered light should not exceed 5% and will in general be much less. Cross sections for ozone absorption and molecular scattering at the wavelengths used in backscattered ultraviolet observations are given in Table 4.

d. *Model Results and Discussion*

The relative importance of chemistry versus transport of ozone can be estimated by comparing the photochemical lifetime of odd oxygen with the effective time scales for transport. As shown in Figures 2 and 5, odd-oxygen in the stratosphere is dominated by ozone; its lifetime is approximately 10 days at 30 km and decreases to less than 1 day at 40 km. On the basis of the time scales for vertical diffusion of trace gases [cf., *Hunten*, 1975; *Logan et al.*, 1978; *Wofsy*, 1978] and the maximum inferred meridional winds [*Leovy*, 1964; *Mahlman and Moxim*, 1978], we do not expect transport of odd-oxygen to play a dominant role in determining the concentrations of O_3 above 35 km. Local photochemical production and loss may even control the ozone density below 35 km when vertical transport is inefficient, for example during summer at mid-latitudes [*Mahlman et al.*, 1980]. The family of odd-hydrogen radicals has a much shorter stratospheric lifetime and will be in photochemical steady state.

Odd oxygen in the upper mesosphere is comprised mostly of atomic oxygen, and its lifetime increases above 75 km, reaching approximately 1 day at 90 km. Important transport

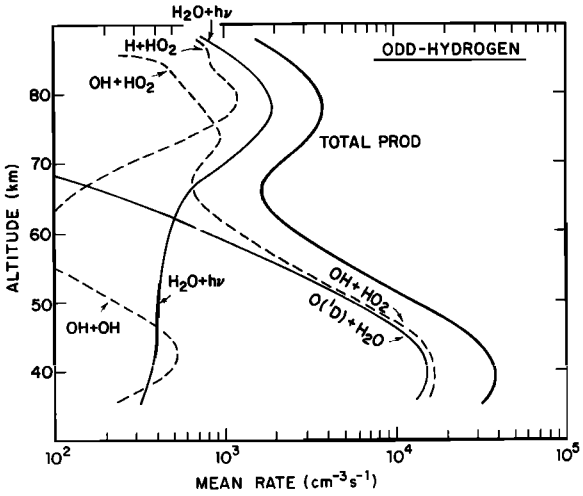

Fig. 4. Vertical profile of mean photochemical rates important to odd-hydrogen. See Figure 3.

of odd oxygen through both tidal displacement vertical mixing [*Keneshea et al.*, 1979] may be expected at these altitudes. The amplitude of the atmospheric tides grows exponentially with altitude, and vertical mixing is rapid, corresponding to an eddy diffusion coefficient of the order of 10^6 cm^2 s^{-1} [*Hunten*, 1975; *Keneshea et al.*, 1979; *Allen et al.*, 1980]. Significant transients are observed in the abundances of atomic oxygen in these regions [*Wasser and Donahue*, 1979]. Odd-hydrogen lifetimes also increase rapidly with altitude above 75 km, and we may no longer presume the HO_x family to be in photochemical steady state above about 80 km.

The concentration of H_2O in the upper stratosphere and mesosphere is very important to the chemical model, but data above 35 km are sparse, and we must rely on stratospheric measurements to place limits on mesospheric H_2O. Our choice for the H_2O profile is constrained by the range of observations as reviewed by *Harries* [1976] and by recent measurements in the tropical stratosphere [*Kuhn*, 1979; *Kley et al.*, 1979]. A uniform mixing ratio of 5 ppmv H_2O is adopted from 30 to 90 km, but values from 2 to 10 ppmv are also considered.

The choice of a uniform mixing ratio for H_2O is based on the assumption that there are no significant sources or sinks for H_2O in the region 35–75 km. In the lower stratopshere the H_2O mixing ratio is expected to increase by 3 ppmv between the tropopause and the stratopause owing to oxidation of CH_4. Above 75 km, H_2O is destroyed by conversion to H_2 through a sequence of reactions beginning with

(R42) $$H_2O + h\nu \rightarrow H + OH$$

and culminating with

(R15) $$H + HO_2 \rightarrow H_2 + O_2$$

The resulting molecular hydrogen is photochemically inert in the mesosphere [*Liu and Donahue*, 1974] except below 60 km where $O(^1D)$ concentrations are sufficient to convert H_2 into odd-hydrogen ((R10)) and subsequently water ((R17)).

Profiles of the trace gases CO, CH_4, H_2, and the chemical families Cl_x and NO_x were derived from *Logan et al.* [1978] and are given in Table 3. Unless otherwise stated, all calculations are for equinoctal conditions with the 15°N atmosphere from the *U.S. Standard Atmosphere Supplements* [1966].

The calculated noontime concentrations of O_3 and O are shown in Figure 5. The sensitivity of the odd-oxygen chemis-

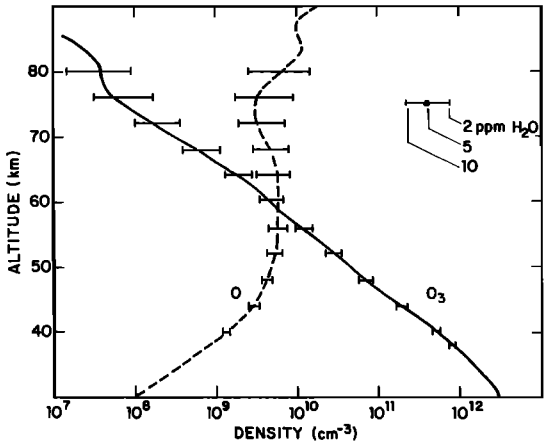

Fig. 5. Vertical profiles of noontime ozone and atomic oxygen. For the standard photochemical model with 15°N annual atmosphere, the horizontal bars show the effect of water vapor (2-5-10 ppm) on the concentrations.

try to the concentration of H_2O increases with altitude. Indeed, a factor of 5 decrease in H_2O above 70 km causes up to an order of magnitude increase in O_3 and O.

The detailed diurnal behavior of ozone with altitude is displayed in Figure 6. Significant day-to-night variations in the concentration of ozone occur above 50 km because the daytime atomic oxygen density is comparable to or greater than that of ozone. The daily cycle of ozone above 70 km exhibits a complex structure with variation of the ozone concentrations in excess of a factor of 2 over the sunlit portion of the day.

The rise in ozone and total odd oxygen begins approximately 20 minutes after sunrise, driven by photolysis of molecular oxygen ((R38)) in the Schumann-Runge bands. Photolysis of H_2O at Lyman-alpha, the source of odd hydrogen above 65 km, is strongly peaked about local noon. The HO_x concentrations maximize in the afternoon, and the ozone density is thus asymmetrical about noon. An increase in the concentration of mesospheric water depresses the mean concentration of ozone and causes the peak daytime concentration to occur earlier in the day. In this photochemical regime, odd oxygen will also be sensitive to changes in solar Lyman-alpha. Such variations are known to occur [*Hinteregger*, 1979] over the solar rotation (~30 days) and over the solar cycle (~11 years; see section 3*g*). Noontime densities of OH and H for the standard model are shown in Figure 7. Also shown is the decrease in OH for 2 ppm H_2O and the increase in OH corresponding to solar maximum.

3. Ozone Observations

a. BUV Satellites

Remote sensing of the earth's atmosphere by satellite provides the only practical means for global monitoring of the constituents of the stratosphere and mesosphere. The ultraviolet spectrometers on the Atmospheric Explorer-E and Nimbus-4 satellites have measured the backscattered solar flux intermittently since 1970. These observations contain a wealth of information about the ozone mixing ratios in the upper atmosphere and provide a primary test of the photochemical model.

TABLE 3. Trace Gas Composition for Standard Model

Constituent	Volume Mixing Ratio
H_2O	5.0 ppm
H_2	0.5 ppm
NO_x (30 km)	6.5 ppb
(40–90 km)	16.0 ppb
Cl_x	2.0 ppb
CH_4 (30–40 km)	0.70 ppm
CO (30–40 km)	0.01 ppm

The AE-E satellite was launched on November 20, 1975, into an equatorial orbit with an inclination of approximately 20°. The orbit of AE-E has been changed from an initial perigee-apogee range of 150–3000 km to a nearly circular orbit at 250 km and eventually raised to a 450 km circular orbit. For an observing pass over the sunlit hemisphere, the backscattered ultraviolet (BUV) instrument is pointed toward the nadir so that it observes the solar flux reflected from the atmosphere in the direction of the zenith. Thus, during a suitable period, the AE-E satellite can observe the BUV radiances from 20°S to 20°N latitude over all longitudes and for all local solar times from sunrise to sunset.

The Nimbus-4 satellite was launched into an 1100 km circular orbit and began BUV operations in April 1970. The satellite orbit is nearly synchronous with local solar time, monitoring local noon conditions on the daylit hemisphere and local midnight on the dark side. Thus, the solar zenith angles represented in the Nimbus-4 observations are restricted to noontime values, and their variation is directly correlated with the seasonally varying declination of the sun.

The BUV spectrometer on both AE-E and Nimbus-4 [*Heath et al.*, 1973] detects the diffuse radiances (erg cm^{-2} s^{-1} $Å^{-1}$ $steradian^{-1}$) with a field of view 12° in diameter and measures the solar irradiance (erg cm^{-2} s^{-1} $Å^{-1}$) by observing the sun through a transmission filter (AE-E) or by measuring light from a diffuse reflector (Nimbus-4). The ratio of backscattered light to solar flux defines a dimensionless BUV albedo (3). The instrument operates in 12 discrete wavelength channels, of which only the five shortest will be considered here: 2555, 2735, 2830, 2876, and 2922 Å. At these wavelengths the BUV albedos are not affected by clouds or by ground albedo. The solar fluxes measured by the AE-E BUV instrument and the relevant molecular cross sections are given in Table 4.

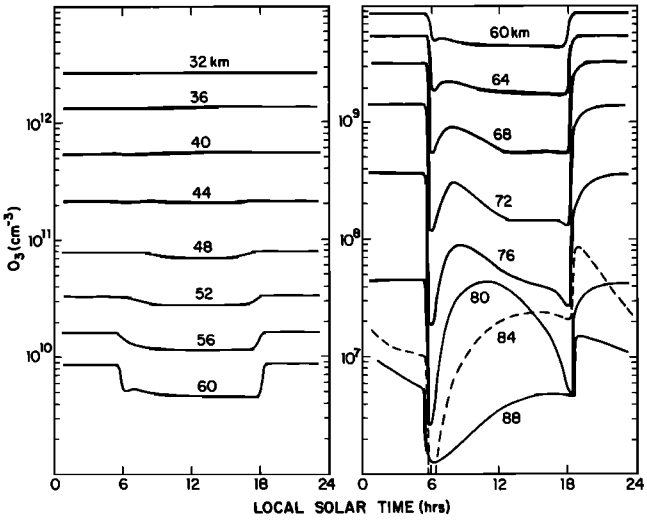

Fig. 6. Diurnal variation of ozone with altitude. The ozone concentrations have been calculated with the standard model under equatorial and equinoctal conditions. The assumption of a local steady state may not be valid below 36 km or above 80 km.

The shorter wavelengths have greater ozone extinction cross sections, and consequently the solar flux is absorbed at high altitudes. The peak contribution to p_λ for the range of wavelengths shown in Figure 8 varies from 40 to 66 km with wavelength and local solar zenith angle. The broad maxima of the sensitivity function dp_λ/dz make it difficult or impossible to determine uniquely the ozone concentration at a specific altitude from a set of BUV albedos. Thus the inversion of BUV data requires a model profile for ozone which introduces some a priori assumptions into the retrieved profiles [cf., *DeLuisi et al.*, 1979].

All the BUV data have been analyzed here in terms of the albedo as a function of the solar zenith angle. In the tropical and subtropical mesosphere, the variation in ozone with season is not great since both the ozone source and sink terms are affected similarly by solar elevation. For the same reason the diurnal variation in ozone tends to follow the solar zenith angle rather than the local time.

b. *Atmospheric Explorer-E Observations*

The Atmospheric Explorer BUV observations began in December 1975 and continued through March 1977, when the BUV instrument failed. The instrument became operational again in December 1978, and observations began anew. The calibrated radiances were calculated from the raw telemetry data with a program supplied by B. Guenther and R. Dasgupta (private communication, 1978). All the AE-E orbits through 1977 which are catalogued to contain BUV short wavelength data have been examined. Those observations which meet the following criteria were selected for study: (1) Observations must be made below 800–1000 km to avoid contamination by particle radiation [*Heath et al.*, 1973]; (2) because of the large acceptance angle of the instrument (12°) the observation altitude must be less than 800 km to limit the field of view to no more than 1.5° in longitude; (3) for local solar zenith angles greater than 80°, observations must be made below 400 km because of the large gradient of BUV with longitude near sunrise/sunset; and (4) the satellite must be pointed to within 3° of the nadir to permit interpretation of the observed BUV as a straightforward function of local solar zenith angle.

The set of AE-E BUV data which fulfills the above requirements consists of 256 orbits with over 11,000 individual observations at each wavelength. Figure 9 presents the statistical frequency of BUV observations for the wavelength 2555 Å; other wavelengths show similar but not identical distributions. Although the month-by-month distribution of BUV observations is irregular—with certain months not represented at all—we see no significant selection effect in latitude versus season. Likewise, the distribution of observations with local solar time is fairly uniform if we average over a 3-month observing period.

The monthly mean albedos observed by Atmospheric Explorer-E are shown in Figures 10–14 for all five wavelengths. The statistical analysis of the AE-E data was performed by fitting the observed albedos to a piecewise linear function of solar zenith angle. The BUV values reported here refer to the midpoints of specific intervals in solar zenith angle.

The calculation of albedo from the spacecraft-observed specific intensities requires knowledge of the solar flux at the time of observation. The eccentricity of the earth's orbit (0.0167) causes a 6.6% variation in the solar flux at the top of the atmo-

TABLE 4. BUV Wavelength Data

λ, Å	F_λ* (Sun at 1 AU), erg $cm^{-2}\ s^{-1}\ Å^{-1}$	$\sigma_\lambda(O_3)$, $\times 10^{-18}\ cm^2$	σ_λ(air), $\times 10^{-26}\ cm^2$
2555	10.8	11.7	11.4
2735	22.8	6.38	8.45
2830	35.8	2.96	7.29
2876	36.3	1.84	6.80
2922	57.1	1.02	6.35

Sources: Second column, B. Guenther (private communication, 1980); third column, *Inn and Tanaka* [1953], *DeMore and Raper* [1964], *Griggs* [1968]; fourth column, *Edlen* [1953], *Penndorf* [1957], *Penney et al.* [1974].

*These solar fluxes are solely for use within the AE-E BUV dataset and are applied here only to determine the BUV albedo.

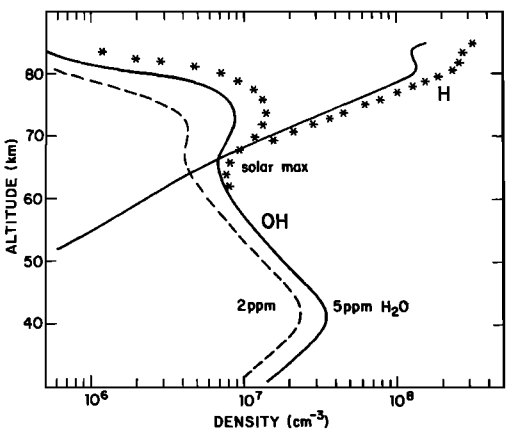

Fig. 7. Vertical profiles of noontime OH and H. The standard model with 5 ppm H_2O is given by the solid line; the model with 2 ppm H_2O, the dashed line; and the model at solar maximum with 5 ppm H_2O, the asterisks.

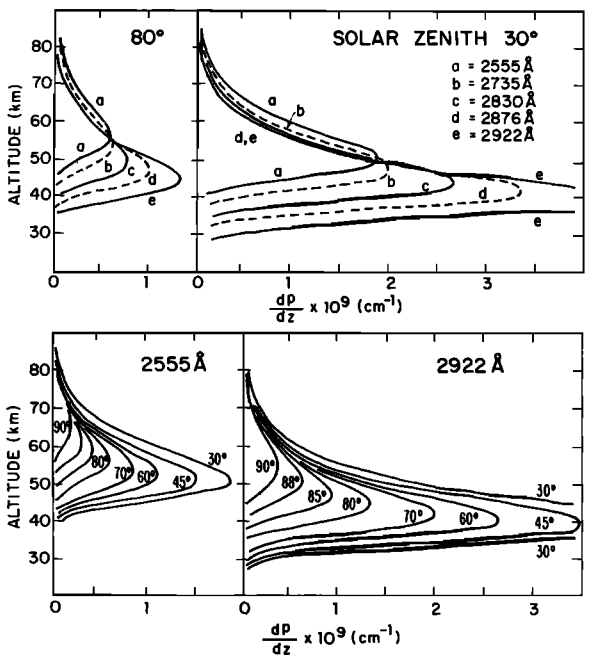

Fig. 8. Contribution to the BUV albedo (p) as a function of altitude. For the fixed ozone profile shown in Figure 5, the absolute contribution to the albedo at the five standard BUV wavelengths is shown for solar zenith angles of 30° and 80°. For the two extreme wavelengths 2555 and 2922 Å, the dominant source region of the backscattered intensity is seen to rise with increasing solar zenith angle.

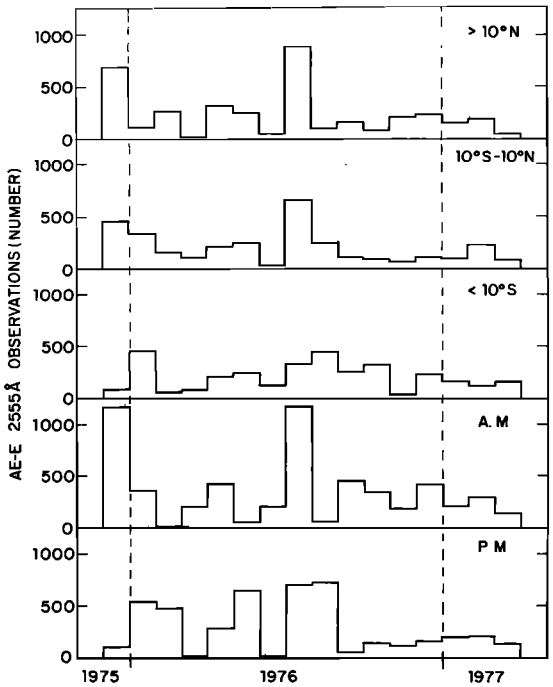

Fig. 9. Monthly statistics for AE-E observations at 2555 Å. The number of acceptable 2555 Å observations in each month of AE-E BUV operations is broken into three latitude bands (10°N-20°N, 10°S-10°N, 20°S-10°S) and also into morning and afternoon. The period of observations is from December 1975 through March 1977.

sphere with a maximum at perihelion in January. In the initial analysis the BUV albedos were computed with a constant mean solar flux as measured by the instrument and given in Table 4. This procedure induces a similarly phased oscillation of 6.6% in the albedos reported in Figures 10–14. In all subsequent comparisons, the variation in solar flux has been included in both the photochemical model and the observed albedos.

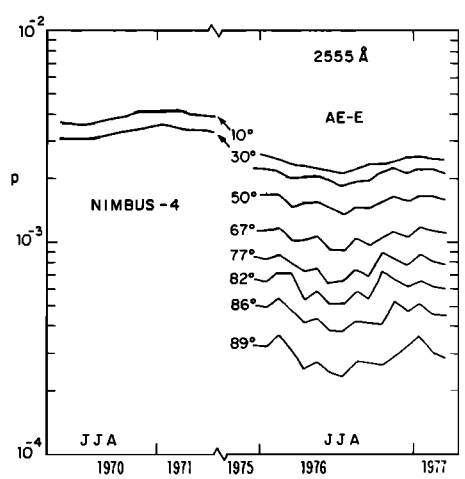

Fig. 10. Monthly mean BUV albedos (p) at 2555 Å. The dimensionless albedo p is defined as 4π (steradian) times the nadir-reflected specific intensity (W cm^{-2} steradian^{-1}) divided by the solar flux (W cm^{-2}). For the albedos shown here, the solar flux was fixed (at 1 AU) and not allowed to vary with sun-earth distance. The mean albedos from Nimbus-4 are based on the tropical data from May 1970 to May 1971 and only give albedos at solar zenith angles of 10° and 30°. The AE-E data span December 1975 through March 1977 and are shown for all solar zenith angles from 10° to 89°. The months June, July, and August are denoted on the abscissa.

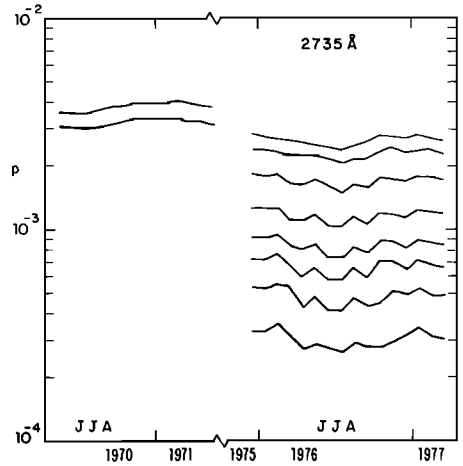

Fig. 11. Monthly mean BUV albedos (p) at 2735 Å. Same as Figure 10.

The period from December 1975 to March 1977 was marked by very low solar activity with a monthly mean flux at 10.7 cm of 67 to 82 and a sunspot number (R_z) of 8 to 23. This may be contrasted with the first year of Nimbus-4 observations which took place during the solar maximum of cycle 20. In the period April 1970 to March 1971, the monthly mean 10.7 cm flux was typically 150 or more, and the monthly sunspot number (R_z) ranged from 61 to 128.

c. *Nimbus-4 Observations*

The Nimbus-4 BUV albedos from the entire first year of observations were made available by A. Fleig and V. G. Kaveeschwar (private communication, 1979). The calculation of the monthly mean albedos as a function of solar zenith angle was performed in the manner described for the AE-E data. Two selection processes are specific to the Nimbus-4 data: (1) only observations between 25°S and 25°N latitude are included, and (2) all data from a substantial region centered over the South Atlantic Ocean have been discarded. Particle radiation above 1000 km causes an excess signal [cf., *Heath et al.*, 1973] which is readily discerned on a latitude-longitude grid and which extends westward from 60°E to 150°W longitude. The tropical Nimbus-4 data are limited to solar zenith angles less than 48°. Thus albedos are reported only for solar zenith angles of 10° and 30°, corresponding to intervals (0°,

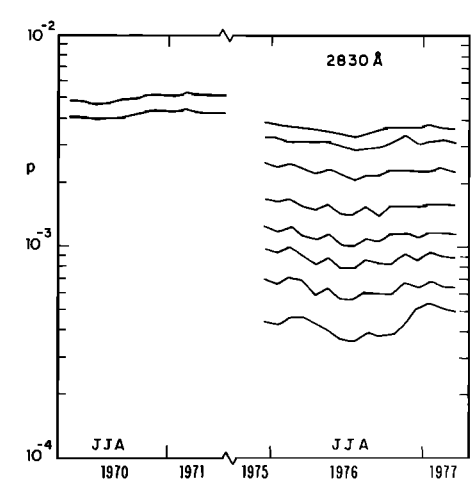

Fig. 12. Monthly mean BUV albedos (p) at 2830 Å. Same as Figure 10.

20°) and (20°, 40°). Each monthly mean albedo shown in Figures 10–14 is based on 800 to 3000 observations.

d. Direct Comparison of BUV Albedos

Two striking features of Figures 10–14 are the systematic difference between the AE-E and Nimbus-4 albedos and the large, apparently annual cycle in the BUV radiances. The Nimbus-4 albedos are consistently 40–60% larger than the AE-E albedos. In spite of efforts to discern the cause of this difference (B. W. Guenther, private communication, 1980) none has been found. As expected, the annual cycle shows the 6.6% solar flux variation but, in many cases, has a larger amplitude. It is seen in both sets of BUV albedos and seems to be associated with the mesosphere above 50 km (i.e., short wavelengths and large solar zenith angles are most strongly affected).

Previous studies of the Atmospheric Explorer BUV [*Frederick et al.*, 1977, 1978; *Frederick*, 1979] considered only small samples of the entire data set. Also, these studies did not discuss the problems associated with the absolute calibration of the AE-E albedos. Published studies of the Nimbus-4 BUV [e.g., *DeLuisi et al.*, 1979] have presented only the inverted ozone profiles and have not analyzed the BUV radiances.

e. Rocket Ozone Observations

Additional ozone data obtained by rocket soundings are available for comparison with model calculations. The rocket ozone project (ROCOZ) launched rockets from Wallops Island, Virginia (38°N) at the rate of one per month during the period March 1976 to March 1979 [*Wright et al.*, 1978; *Krueger and Wright*, 1979]. The optical ozonesonde used in these flights measured the attenuation of solar flux at four wavelength channels between 2500 and 3200 Å as the instrument descended on a parachute from its release at 58–70 km. The observed extinction of sunlight provides a measure of the ozone number density above the altitude of the ozonesonde.

The average profile for ozone from 32 to 58 km as reported by Wright [*Krueger and Wright*, 1979] is shown in Figure 15 along with two theoretical profiles of noontime ozone. The modeled distributions represent the mean of profiles computed for the January, April, July, and October 30°N atmospheres [*Cole and Kantor*, 1978]. The standard photochemical model diverges from the observed profile above 40 km. However, the model with only 2 ppm H_2O agrees well with the ROCOZ data, predicting uniformly 8% less ozone over the range of 5 scale heights in ozone density.

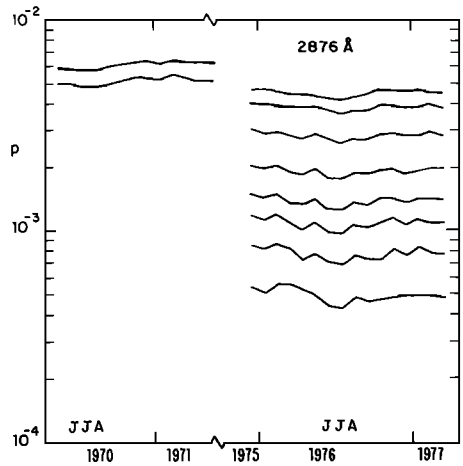

Fig. 13. Monthly mean BUV albedos (p) at 2876 Å. Same as Figure 10.

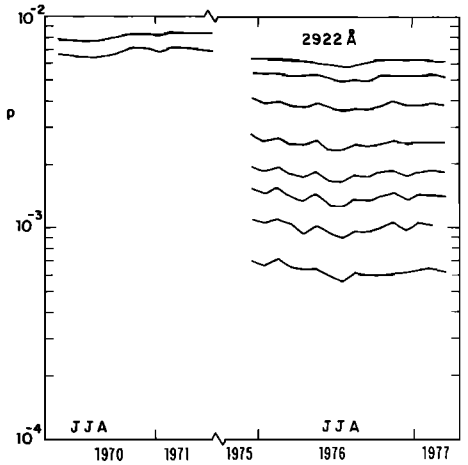

Fig. 14. Monthly mean BUV albedos (p) at 2922 Å. Same as Figure 10.

The annual variation of ozone at Wallops Island is displayed in Figure 16. Concentrations of ozone observed for each season are satisfactorily reproduced by the model above 40 km where the photochemical lifetime of ozone is less than 1 day. The calculated seasonal differences at these altitudes are due mainly to the structure of the background atmosphere. For example, if ozone mixing ratios were to be plotted against pressure, winter O_3 would exceed summer O_3 between 0.8 and 3 mbar (~40 to 50 km) with the reverse true above 0.8 mbar. Below 40 km the model fails to predict the observed spring maximum and fall minimum. This discrepancy may be due either to the poorly characterized mean reference atmosphere or to the large rates of ozone transport, as seen in the models of *Mahlman et al.* [1980].

f. Absolute Calibration of AE-E Albedos

Figure 17 shows a comparison between the BUV albedos from AE-E and Nimbus-4 with those calculated from the ROCOZ data. The figure includes also albedos derived from a daytime ozone profile by *Hilsenrath* [1971] and from high-altitude twilight ozone profiles measured by solar occultation with the AE-E BUV instrument [*Guenther et al.*, 1977]. The low ultraviolet albedos observed by AE-E disagree with all the other data shown in Figure 17 and cannot be explained in terms of any reasonable theoretical model. While only the occultation studies truly overlap with the AE-E BUV data, the midlatitude ROCOZ observations were made during the same period, and the Nimbus-4 albedos cover the same tropical regions at an ealier time. This evidence strongly suggests the possibility of a systematic error in the AE-E ratio of backscattered radiance to solar irradiance. The ratios of AE-E to Nimbus-4 BUV are (0.62, 0.70, 0.73, 0.74, and 0.75) for the wavelengths (2555, 2830, 2876, and 2922 Å) at a solar zenith angle of 30°. A reduction of this magnitude in BUV albedo corresponds to a factor of 2 enhancement in ozone concentrations.

g. Response to Solar Variations

The response of the atmosphere to changes in the incident solar flux is complex and may alter the distribution of ozone. In addition to the annual cycle in total flux, the sun is observed to vary over time scales corresponding to solar rotation

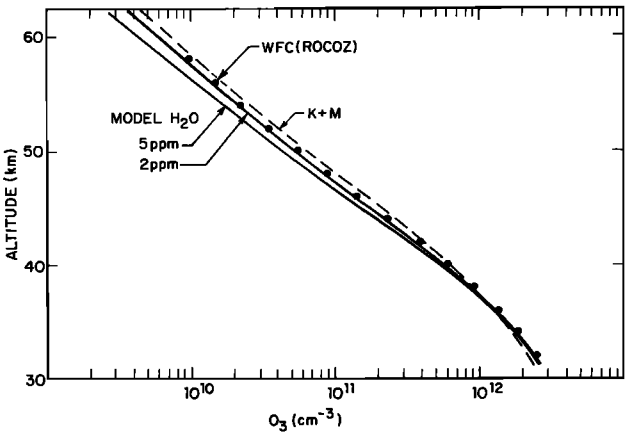

Fig. 15. Mid-latitude ozone profiles. Two modeled ozone profiles are compared with the 3-year mean ozone concentrations from the ROCOZ project [*Krueger and Wright*, 1979] and with the *Krueger and Minzner* [1976] mid-latitude model. The model values represent a four season mean of noontime ozone concentrations computed by using the standard photochemical model in Table 1 for 30°N atmospheres with both 2 and 5 ppm volume mixing ratio of H_2O.

(30 days) and to the solar cycle (11 years). Flux variations during the latter two phenomena depend strongly on wavelength as shown in Figure 18. The present analysis considers only the direct effect of flux variations on the photochemistry and assumes an unchanging atmospheric structure.

The 11-year solar cycle may contribute to the systematically different BUV albedos observed by AE-E (solar minimum) and Nimbus-4 (solar maximum). Data on the variation of solar flux previous to cycle 21 are sparse and are sometimes contradictory [*Simon*, 1978]. Such data from solar cycle 20 have been used in previous studies [*Penner and Chang*, 1978; *Callis et al.*, 1979] to postulate significant variability in the solar flux shortward of 3000 Å. Recently, *Hinteregger* [1979] reported observations of solar cycle 21 which were made continuously from July 1976 to January 1979 and are summarized in Figure 18. His results indicate a factor of 2.8 variation at Lyman-alpha but only a 20% increase in solar flux at 1800 Å. Hinteregger's observations have been extrapolated to 2000 Å and are assumed to represent the variation in solar flux between the

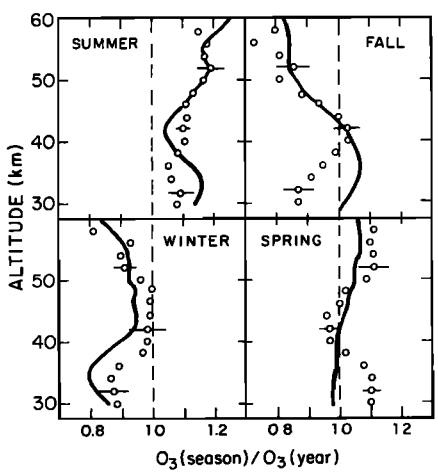

Fig. 16. Seasonal variation of ozone. The relative seasonal variation of ozone at mid-latitudes from the ROCOZ data (dots) is compared with results from the standard photochemical model with 30°N seasonal atmospheres (solid lines). The annual means are shown in Figure 15. Typical errors for the data points are given.

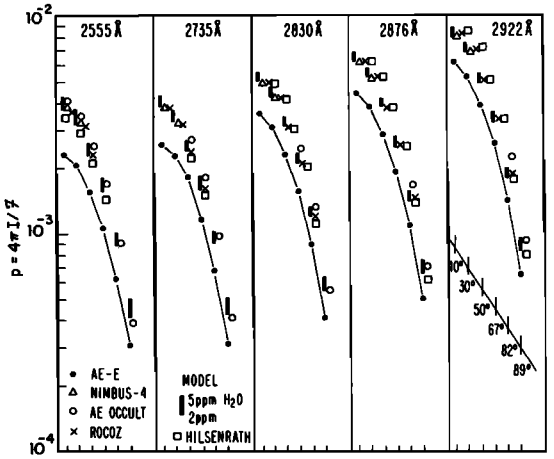

Fig. 17. BUV albedos at five wavelengths for specific solar zenith angles. For each of the five standard BUV wavelengths, the mean AE-E albedos are shown for solar zenith angles from 10° to 89° (dots connected by line). The mean tropical Nimbus-4 albedos are given for zenith angles of 10° and 30° only (triangles). BUV albedos have been calculated for the observed ozone profiles from ROCOZ (crosses), from *Hilsenrath* [1971] (squares), and from solar occultation with the AE-E instrument [*Guenther et al.*, 1977] (circles). These albedos are shown only for the relevant wavelengths and the zenith angles. The albedos from the standard photochemical model (Table 1) for a range of H_2O mixing ratios (2–5 ppm) are given for all wavelengths at all angles (vertical bars).

1970–1971 Nimbus-4 BUV and the 1975–1977 AE-E BUV data.

The predominant effects at solar maximum are due to the increased solar radiation at Lyman-alpha and have little effect on the ozone concentrations below 60 km. At solar maximum the odd hydrogen concentrations are greatly enhanced (Figure 7), and ozone is depleted by 25 and 50% at altitudes of 70 and 80 km, respectively. Some caution is necessary since the greater rate of H_2O photolysis will enhance the conversion of H_2O to H_2. Depending on the rate of vertical transport [*Keneshea et al.*, 1979; *Allen et al.*, 1980], the H_2O concentration at 80 km may fall below 3 ppm, thus canceling the predicted ozone depletions. Assuming fixed H_2O profiles, the model predicts greater albedos at solar maximum, at most 1.5% for the shorter wavelengths near sunset. The effect for solar zenith angles less than 40° would be below 0.5%. Thus changes in the solar flux associated with the 11-year solar cycle do not appear by themselves to produce a detectable variation in ozone

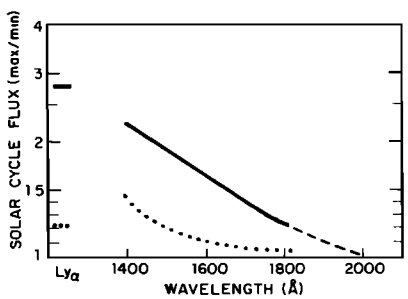

Fig. 18. Variation in ultraviolet solar flux. The ratio of solar flux near solar maximum (January 1979) to that at solar minimum (July 1976) has been observed by *Hinteregger* [1979]; the observations at Lyman-alpha and from 1400 to 1800 Å (solid line) have been extrapolated to 2000 Å (dashed line). The amplitude of short period (10 day) changes is indicated by the dotted line [*Hinteregger*, 1979].

TABLE 5. Ratio of AE-E BUV Albedos to Photochemical Model Albedos at Solar Zenith Angles of 30°/86°

Wavelength, Å	Standard Model			Dry Model		
	January 1976	July 1976	January 1977	January 1976	July 1976	January 1977
2555	0.58/0.63	0.53/0.56	0.57/0.59	0.64/0.72	0.60/0.64	0.63/0.67
2735	0.61/0.65	0.59/0.60	0.61/0.61	0.68/0.74	0.65/0.68	0.67/0.69
2830	0.64/0.67	0.62/0.62	0.63/0.62	0.70/0.75	0.68/0.70	0.68/0.69
2876	0.66/0.67	0.64/0.63	0.64/0.62	0.71/0.75	0.69/0.70	0.69/0.69
2922	0.69/0.67	0.67/0.64	0.66/0.62	0.73/0.73	0.72/0.70	0.71/0.68

The standard photochemical model (5 ppm H_2O) is described by Tables 1, 2, and 3. The dry model with 2 ppm H_2O is also equivalent to the standard model with $k_{17} = 1 \times 10^{-10}$ cm^3 s^{-1}. The BUV albedos used in this table are the average of the morning and afternoon albedos. While shown for only 30° and 86°, the ratio of albedos is a smoothly varying function of zenith angle from 10° to 89°.

because any significant changes in ozone would occur above the altitudes efficiently probed by BUV. Solar UV variations associated with the rotation of an active solar region (see Figure 18) are smaller than those associated with the solar cycle and will likewise be undetectable by BUV. The observed 5% r.m.s. variation in the monthly mean BUV radiances places an upper limit both on the natural variation of ozone with longitude and time and on the short-term variability in solar flux between 2555 and 2922 Å.

h. *Detailed Comparison with Theory*

A detailed comparison of the Nimbus-4 albedos with those from two theoretical models is shown in Table 6. The standard photochemical model appears to underestimate the quantity of ozone and thus overestimates the BUV irradiances by 9–16%. The dry theoretical model provides much better agreement but is still 5% greater than the observed albedos. The Nimbus-4 2555 Å albedo is anomalously higher than the other wavelengths when they are compared with the dry model. In view of the strong overlap in regions sampled by the BUV (Figure 8), the 5% excess at 2555 Å is difficult to explain. A possible explanation could be the occurrence of an error of equal magnitude in the ozone cross section at 2555 Å (Table 4), but the cross section at this wavelength has been measured several times [*Griggs*, 1968].

Resonance fluorescence by nitric oxide has been proposed as a source of contamination in the 2555 Å BUV albedos [*Guenther et al.*, 1979]. A substantial fraction of the sunlight at 2150 Å is reradiated in the $(v', v'') = (1, 4)$ gamma band near 2555 Å. *Guenther et al.* [1979] note that the major contribution is from thermospheric NO and that it may be as large as 5% of the BUV signal at high latitudes. In the tropics, however, thermospheric NO densities are typically 5 times less than those observed at high latitudes [*Cravens and Stewart*, 1978]. Thus the nitric oxide contribution to the tropical 2555 Å radiances should be less than 1% for daytime observations.

At this point we can compare the ROCOZ data from 38°N with the Nimbus-4 tropical data. Both sets of observations present a consistent pattern which is well described by a standard photochemical model with 2 ppm H_2O or, equivalently, with $k_{17} = 1 \times 10^{-10}$ cm^3 s^{-1}. This model reproduces the observed ozone scale height from 35 to 55 km and predicts concentrations within 5–10% of those observed.

The BUV data from Atmospheric Explorer-E require more detailed analysis. They contain important diagnostics, if we can assume that the relative changes in BUV intensities throughout the day are accurate. The BUV albedos decrease by a factor of 9 with solar zenith angle from 10° to 89°. The rate of this diminution is a measure of the ozone scale height and provides a test of the theoretical model from 40 to 70 km. In Table 5 the AE-E albedos from noon to twilight are compared with theoretical albedos computed for the correct solar distance and seasonal atmosphere [*Cole and Kantor*, 1978]. These observations have been averaged at complementary morning and afternoon zenith angles to eliminate the effects of an ephemeris error.

To achieve a statistically significant number of observations at large zenith angles, the AE-E data have been grouped into 3-month periods centered on January 1976, July 1976, and January 1977. These time periods span the useful range of this set of AE-E data and represent the successive maximum-minimum-maximum which are observed in the backscattered light. This annual cycle seen in Figures 10–14 is now visible only at 2555 Å; the remaining wavelengths exhibit a discontinuity in the albedos between January 1976 and July 1976.

The decrease in BUV albedo with solar zenith angle is reproduced to within 6% by the theoretical models. The standard photochemical model matches the diurnal behavior of the shorter wavelengths, whereas the dry model is more representative of the longer wavelengths. One possible conclusion is that from 50 to 60 km either the H_2O mixing ratio increases from 2 to 5 ppm or else the rate constant for $OH + HO_2$ (R17) decreases by the same factor. The anomalous period January 1976 is consistent with a much wetter stratosphere (~8 ppm H_2O).

The asymmetry in the daytime ozone concentrations shown in Figure 6 leads to a morning-afternoon difference in the backscattered ultraviolet which should be observed by satellite. In Figure 19 the modeled ratio of afternoon-to-morning backscattered light is compared with values from the three periods of AE-E data. Potentially large, systematic shifts in these ratios can be caused by an ephemeris error as small as 3 s. The model predicts less than 1% difference between the corre-

TABLE 6. Ratio of Nimbus-4 BUV Albedos to Photochemical Model Albedos

Wavelength, Å	Standard Model		Dry Model	
	July 1970	January 1971	July 1970	January 1971
2555	0.87	0.91	0.98	1.02
2735	0.85	0.86	0.94	0.95
2830	0.86	0.88	0.93	0.95
2876	0.88	0.90	0.95	0.97
2922	0.88	0.90	0.94	0.96

The models are described in Table 5. The Nimbus-4 BUV albedos are from the periods June–August 1970 and December 1970 to February 1971. The values represent the mean of ratios at solar zenith angles 10° and 30°. The typical month-to-month variation in the mean Nimbus-4 albedo at 30° zenith angle is ±2%.

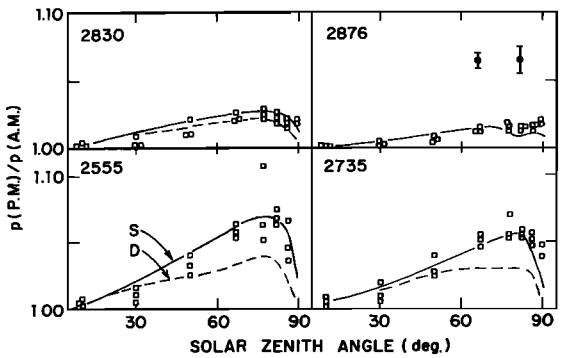

Fig. 19. Ratio of AE-E afternoon albedo to morning albedo. The P.M.-to-A.M. ratio of BUV albedos at the same solar zenith angle is calculated relative to an assumed 2922 Å ratio of unity. The dots represent AE-E data for the periods January 1976, July 1976, and January 1977, as described in the text. The theoretical curves refer to the standard (S) and dry (D) models.

sponding morning and afternoon albedos at 2922 Å; thus, the 2922 Å albedo has been used to locate precisely the time of observation (e.g., the 2876 Å observation occurs 2 s after 2922 Å and so on). The AE-E data have the same P.M./A.M. patterns as the photochemical model and one cannot readily distinguish between models with 2 to 5 ppm H_2O. The P.M./A.M. ratios from January 1976 are indistinguishable from the other periods.

The AE-E observations point to an annual cycle in the 2555 Å albedo, notably at large zenith angles. There is a January maximum and July minimum at short wavelengths which is only partially explained by the model through seasonal changes in the background atmosphere [*Cole and Kantor,* 1978]. The reduced albedo during the months of June, July, and August appears also in the Nimbus-4 data; however, the pattern may not extend to July 1971 (P. K. Bhartia, private communication, 1980). This indication of a July maximum in the ozone absorption above 40 km differs from the mid-latitude results of *DeLuisi et al.* [1979]. They analyzed inverted ozone profiles for the same period of Nimbus-4 observations and infer a summer minimum in ozone (pressure versus pressure) above 40 km for 36°N to 52°N. The mid-latitude rocket observations (38°N) show everywhere a summer maximum in ozone density versus altitude. The model which fits the ROCOZ data implies, however, a summer minimum in ozone partial pressure versus total pressure between 40 and 50 km. Thus the July minimum in shortwavelength albedos in the tropics will become a July maximum by northern mid-latitudes. Above 50 km, by any manner of comparison, the Nimbus-4 radiances analyzed here (25°S to 25°N) and the Wallops Flight Center (38°N) ROCOZ data are in harmony with the AE-E data and imply a mesopheric maximum in July from 25°S to 38°N.

While the three sets of ozone data presented in this paper are reasonably consistent and show overall agreement with the model, not all observations of ozone support this view. For example, the several midnight ozone profiles deduced from stellar occultations by the Copernicus satellite [*Riegler et al.,* 1977] do not agree at all with the model results. These nighttime observations cannot be compared directly with the daytime observations except through the photochemical model. In this case, the Copernicus ozone densities are a factor of 2 larger than the densities from any of the models discussed here and remain controversial [*Gille et al.,* 1980]. Another case of disagreement between data sets can be seen by comparison of *Watanabe and Tohmatsu's* [1976] seasonal ozone dependence with that of *Krueger and Wright* [1979]. Between 40 and 55 km, Watanabe and Tohmatsu (31°N, Japan) report a winter to summer ozone ratio of approximately 2; whereas Krueger and Wright (38°N, Wallops Island) observe a modest excess (10–30%) of summer ozone over winter ozone (density versus altitude). A separate test of the photochemical model is provided by in situ observations of atomic oxygen in the region 60–80 km [*Dickinson et al.,* 1980]. Daytime observations are limited and few (e.g., three profiles at 57°N winter) but are adequately described by the theoretical model with 2 ppm H_2O (see Figure 5).

4. Discussion

The three sets of ozone data which are analyzed in this paper present a reasonably coherent view of ozone in the upper atmosphere. The absolute calibration of the AE-E albedos is anomalous, but their diurnal structure and symmetry are consistent with the ROCOZ profiles and Nimbus-4 albedos. The AE-E BUV data are the only set of continuous observations which are sensitive to ozone above 55 km in the tropics. With the renewed availability of the AE-E instrument, the issue of absolute calibration may be resolved by simultaneous overpasses of AE-E BUV and Nimbus-7 SBUV/TOMS.

The short wavelength AE-E data suggest the existence of an annual cycle in tropical ozone above 50 km. There is an unexplained 6% excess of January albedos over July albedos at 2555 Å and a possible excess at 2735 Å. Several explanations for excess ozone in July may be hypothesized. One approach is to invoke variable water vapor concentrations above 55 km with a minimum in July. Another is to hypothesize large-scale variations in thermospheric ozone between 85 and 105 km (M. B. McElroy, private communication, 1980); these variations would have to be of the order of 10^{15} ozone molecules cm^{-2}, which is as large as the entire nighttime thermospheric ozone column [*Riegler et al.,* 1977]. Also, if the reactions O + OH (R4) and O + HO_2 (R5) depend on temperature, then they might proceed more slowly in the colder July atmosphere above 60 km. For modest activation energies [cf. *Logan et al.,* 1978], the resulting increase in ozone could explain half of the observed excess in the annual cycle. As was noted before [Guenther et al., 1979], resonance fluorescence of nitric oxide contributes to the observed intensities at 2555 Å; the 5% annual variation would correspond to a yearly cycle of order 4×10^{15} NO cm^{-2} above 50 km. Since thermospheric NO in the tropics is observed to vary by only 1×10^{14} cm^{-2} [*Stewart and Cravens,* 1978], such a cycle would require unusually large variations (~100 ppb) in mesospheric NO [cf. *Hudson and Reed,* 1979, p. 173].

A major uncertainty in the photochemical model for ozone centers on the kinetic data for the reaction OH + HO_2 (R17). Measurements at low pressures [*Burrows et al.,* 1977; *Chang and Kaufman,* 1978] give $k_{17} \simeq 4 \times 10^{-11}$ cm^3 s^{-1}, while the reaction appears to be much faster at 1 atm [*DeMore,* 1979], $k_{17} \simeq 1 \times 10^{-10}$ cm^3 s^{-1}. Excellent modeling of the ozone observations is achieved within this range of kinetic measurements. The ozone data indicate a possible transition in k_{17} between 50 and 60 km (0.7–0.3 torr). Similarly, an acceptable model of mesospheric CO observations is possible with the lower value of k_{17} near 80 km [*Allen et al.,* 1980]. The sensitivity of the photochemistry to the abundance of H_2O makes mesospheric water measurements an essential part of any refinement in the

theoretical model. Such observations must be devised not only to determine the mean profile of water vapor but also to detect annual short term variability, for example from meteoritic sources.

The photochemical lifetime of $(O + O_3)$ is less than 1 day between 40 and 80 km. Thus the response of ozone to changes in the composition and structure of the atmosphere will be rapid. Global monitoring of ozone in the upper stratosphere and mesosphere provides information not only on long-term trends in the concentration of ozone but also on rapid changes in the composition and structure of the upper atmosphere. To interpret the latter, we must increase our confidence in the photochemical modelling of ozone through continued in situ measurements of ozone by rocket and balloon.

Observations of ozone in the upper stratosphere and mesosphere on a global scale are best accomplished by satellite BUV observations at selected wavelengths between 2200 and 2950 Å. The instrument should have a narrow field of view (1°–3°) and be placed in a circular orbit below 800 km. The orbit must include timely coverage of the full range of local solar zenith angles at a given latitude. The geometric simplicity of nadir observations does not place stringent requirements on the pointing accuracy, makes the analysis of large data sets straightforward and also allows for rapid observations (1 s) of small-scale horizontal structures (8 km) in the atmosphere. Such an instrument must also be able to take advantage of solar and stellar occultations by the atmosphere in order to measure twilight and nighttime ozone profiles.

Acknowledgments. This research was supported by NASA contract NAS-5-24134. A debt of gratitude is due to the entire Atmospheric Explorer Team and its project scientist N. W. Spencer for support and encouragement during this research. The author would like to acknowledge the generosity of many scientists in making their data available: the AE-E BUV radiances were supplied by B. Guenther and R. Dasgupta; the ROCOZ data were reported by D. U. Wright and A. J. Krueger; the first year of Nimbus-4 albedos, by A. Fleig and V. G. Kaveeshwar; and the solar variability measurements were reported by H. Hinteregger. The author is grateful for the constructive support of his colleagues, J. A. Logan, M. B. McElroy, and S. C. Wofsy. C. Spivakovsky aided in the analysis of Nimbus-4 data, and F. F. Zingale provided editorial support. Major computational support was provided by NASA Ames Research Center.

REFERENCES

Allen, M., Y. L. Yung, and J. Waters, Vertical transport and photochemistry in the terrestrial mesosphere and lower thermosphere (50–120 km), *J. Geophys. Res.*, in press, 1980.

Bates, D. R., and M. Nicolet, The photochemistry of atmospheric water vapor, *J. Geophys. Res., 55,* 301–327, 1950.

Baulch, D. L., D. D. Drysdale, D. G. Horne, and A. C. Lloyd, Homogeneous gas phase reactions of the H_2-O_2 system, in *Evaluated Kinetic Data for High Temperature Reactions,* vol. 1, Butterworths, London, 1972.

Baulch, D. L., R. A. Cox, R. F. Hampson, Jr., J. A. Kerr, J. Troe, and R. T. Watson, Evaluated kinetic and photochemical data for atmospheric chemistry, *J. Phys. Chem. Ref. Data, 9,* 295–471, 1980.

Burrows, J. P., G. W. Harris, and B. A. Thrush, Rates of reaction of HO_2 with HO and O studied by laser magnetic resonance, *Nature, 267,* 233–234, 1977.

Callis, L. B., M. Natarajan, and J. E. Nealy, Ozone and temperature trends associated with the 11-year solar cycle, *Science, 204,* 1303–1306, 1979.

Chandrasekhar, S., *Radiative Transfer,* Dover, New York, 1960.

Chang, J., and F. Kaufman, Upper bound and probably value of the rate constant of the reaction $OH + HO_2 \rightarrow H_2O + O_2$, *J. Chem. Phys., 82,* 1683–1687, 1978.

Chapman, S., A theory of upper-atmosphere ozone, *Mem. R. Meteorol. Soc., 3,* 103–125, 1930.

CIAP, The effects of stratospheric pollution by aircraft, in Climatic Impact Assessment Program, Report of Findings, *Rep. DOT-TST-75-70,* Dep. of Trans., Washington, D. C., 1974.

Cole, A. E., and A. J. Kantor, Air Force Reference Atmospheres, *AFGL-TR-78-0051,* U.S. Air Force, Location, 1978.

Cravens, T. E., and A. I. Stewart, Global morphology of nitric oxide in the lower E region, *J. Geophys. Res., 83,* 2446–2452, 1978.

DeLuisi, J. J., C. L. Mateer, and D. F. Heath, Comparison of seasonal variations of upper stratospheric ozone concentration revealed by Umkehr and Nimbus 4 BUV observations, *J. Geophys. Res., 84,* 3728–3732, 1979.

DeMore, W. B., Reaction of HO_2 with O_3 and the effect of water vapor on HO_2 kinetics, *J. Phys. Chem., 83,* 1113–1118, 1979.

DeMore, W. B., and O. Raper, Hartley band extinction coefficients of ozone in the gas phase and in liquid N_2, CO and Ar, *J. Phys. Chem., 68,* 412–414, 1964.

Dickinson, P. H. G., W. C. Bain, L. Thomas, E. R. Williams, D. B. Jenkins, and N. D. Twiddy, The determination of the atomic oxygen concentration and associated parameters in the lower ionosphere, *Proc. Roy. Soc. London, Ser. A., 369,* 379–408, 1980.

Edlen, B., The dispersion of standard air, *J. Opt. Soc. Am., 43,* 339–344, 1953.

Forbes, J. M., and H. B. Garrett, Theoretical studies of atmospheric tides, *Rev. Geophys. Space Sci., 17,* 1951–1981, 1979.

Frederick, J. E., The behavior of tropical ozone during the stratospheric warming of March-April 1976, *J. Atmos. Sci., 36,* 529–540, 1979.

Frederick, J. E., and R. D. Hudson, Dissociation of molecular oxygen in the Schumann-Runge bands, *J. Atmos. Sci., 37,* 1099, 1980.

Frederick, J. E., P. B. Hays, B. W. Guenther, and D. F. Heath, Ozone abundances in the lower mesosphere deduced from backscattered solar radiances, *J. Atmos. Sci., 34,* 1987–1994, 1977.

Frederick, J. E., B. W. Guenther, P. B. Hays, and D. F. Heath, Ozone profiles and chemical loss rates in the tropical stratosphere deduced from BUV measurements, *J. Geophys. Res., 83,* 953–958, 1978.

Gille, J. C., G. P. Anderson, and P. L. Bailey, Comparison of near coincident LRIR and OAO-3 measurements of equatorial night ozone profiles, *Geophys. Res. Lett., 7,* 525–528, 1980.

Griggs, M., Absorption coefficients of ozone in the ultraviolet and visible region, *J. Chem. Phys., 49,* 857–859, 1968.

Guenther, B., R. Dasgupta, and D. Heath, Twilight ozone measurement by solar occultation from AE5, *Geophys. Res. Lett., 4,* 434–436, 1977.

Guenther, B., R. D. McPeters, and J. E. Frederick, A technique for determining daytime atmospheric nitric oxide from BUV measurements, *NASA TM-80325,* 1979.

Hack, W., H. G. Wagner, and K. Hoyermann, Reaktionen von H mit HO_2, I., *Ber. Bunsenges. Phys. Chem., 82,* 713, 1978.

Hack, W., A. W. Preuss, H. G. Wagner, and K. Hoyermann, Reaktionen von Wasserstoffatomen mit Hydroperoxylradikalen, 2, *Ber Bunsenges. Phys. Chem., 83,* 212–217, 1979.

Hampson, J., Photochemical behavior of the ozone layer, *Can. Res. Develop. Estab.,* 1627/4, 1964.

Harries, J. E., The distribution of water vapor in the stratosphere, *Rev. Geophys. Space Phys., 14,* 565, 1976.

Heath, D. F., C. L. Mateer, and A. J. Krueger, The Nimbus-4 backscatter ultraviolet (BUV) atmospheric ozone experiment, two years operation, *Pure Appl. Geophys., 106-108,* 1238–1253, 1973.

Heath, D. F., E. Hilsenrath, B. M. Schlesinger, and V. Kaveeschwar, A preliminary estimate of the seasonal and interannual variations of total ozone for 1970–1975, as derived from BUV, *Eos Trans. AGU, 60,* 268, 1979.

Hilsenrath, E., Ozone measurements in the mesosphere and stratosphere during two significant geophysical events, *J. Atmos. Sci., 28,* 295–297, 1971.

Hinteregger, H., Preliminary data from EUVS experiment on AE-E satellite, paper presented at NASA/AAS Symposium on the Study of the Solar Cycle from Space, Wellesley College, Mass., 1979.

Hudson, R. D., and E. I. Reed, The Stratosphere: Present and Future, *NASA Ref. Publ. 1049,* 1979.

Hunt, B. G., Photochemistry of ozone in a moist atmosphere, *J. Geophys. Res., 71,* 1385–1398, 1966.

Hunten, D. M., Vertical transport in atmospheres, in *Atmospheres of Earth and the Planets,* edited by B. M. McCormac, D. Reidel, Hingham, Mass., 1975.

Hyatt, H. A., J. M. Cherlow, W. R. Fenner, and S. P. S. Porto, Cross

section for the Raman effect in molecular nitrogen gas, *J. Opt. Soc. Am., 63,* 1604–1606, 1973.

Inn, E. C. Y., and Y. Tanaka, Absorption coefficients of ozone in the ultraviolet and visible regions, *J. Opt. Soc. Am., 43,* 870, 1953.

Keneshea, T. J., S. P. Zimmerman, and C. R. Philbrick, A dynamic model of the mesosphere and lower thermosphere, *Planet Space Sci., 27,* 385–401, 1979.

Kley, D., E. J. Stone, W. R. Henderson, J. W. Drummond, W. J. Harrop, A. L. Schmeltekopf, T. L. Thompson, and R. H. Winkler, In situ measurements of the mixing ratio of water vapor in the stratosphere, *J. Atmos. Sci., 36,* 2513, 1979.

Krueger, A. J., and R. A. Minzner, A mid-latitude ozone model for the 1976 U.S. Standard Atmosphere, *J. Geophys. Res., 81,* 4477–4481, 1976.

Krueger, A. J., and D. U. Wright, Some results from rocket ozone (ROCOZ) soundings at Wallops Island, Va., *EOS Trans. AGU, 60,* 268, 1979.

Kuhn, P. M., U-2 water vapor burden observations through the tropopause, in 1977 Intertropical Convergence Zone Experiment, edited by I. G. Poppoff, W. A. Page, and A. P. Margozzi, *NASA TM-78577,* 1979.

Leovy, C., Simple models for thermally driven mesospheric circulation, *J. Atmos. Sci., 21,* 327–341, 1964.

Lindzen, R. S., Atmospheric tides, *Ann. Rev. Earth Planet. Sci., 7,* 199–225, 1979.

Liu, S. C., and T. M. Donahue, The aeronomy of hydrogen in the atmosphere of the earth, *J. Atmos. Sci., 31,* 1118–1136, 1974.

Logan, J. A., M. J. Prather, S. C. Wofsy, and M. B. McElroy, Atmospheric chemistry: Response to human influence. *Phil. Trans. R. Soc., A290,* 187–234, 1978.

Mahlman, J. D., and W. J. Moxim, Tracer simulation using a global general circulation model: Results from a mid-latitude instantaneous source experiment, *J. Atmos. Sci., 35,* 1340–1374, 1978.

Mahlman, J. D., H. Levy, II, and W. J. Moxim, Three-dimensional tracer structure and behavior as simulated in two ozone precursor experiments, *J. Atmos. Sci., 37,* 655–685, 1980.

Murgatroyd, R. J., and F. Singleton, Possible meridional circulations in the stratosphere and mesosphere, *Q. J. R. Meteorol. Soc., 87,* 137–158, 1961.

National Academy of Sciences, Stratospheric ozone depletion by halocarbons: Chemistry and transport, Panel on Stratospheric Chemistry and Transport, Nat. Res. Council, 1979.

NASA-JPL, *Chemical Kinetic and Photochemical Data for Use in Stratospheric Modelling, JPL Publ. 79-27,* Jet Propul. Lab., Pasedena, Calif., 1979.

Penndorf, R., Tables for the refractive index for standard air, *J. Opt. Soc. Am., 47,* 176–182, 1957.

Penner, J. E., and J. S. Chang, Possible variations in atmospheric ozone related to the eleven year solar cycle, *Geophys. Res. Lett., 5,* 817–820, 1978.

Penney, C. M., R. L. St. Peters, and M. Lapp, Absolute rotational Raman cross sections for N_2, O_2 and CO_2, *J. Opt. Soc. Am., 64,* 712–716, 1974.

Prather, M. J., Solutions of the inhomogeneous Rayleigh scattering atmosphere, *Astrophys. J., 192,* 787–792, 1974.

Riegler, G. R., S. K. Atreya, T. M. Donahue, S. C. Liu, B. Wasser, and J. F. Drake, UV stellar occultation measurements of nighttime equatorial ozone, *Geophys. Res. Lett., 4,* 145–148, 1977.

Simon, P. C., Irradiation solar flux measurements between 120 and 400 nm, Current position and future needs, *Planet. Space Sci., 26,* 355–365, 1978.

Stewart, A. I., and T. E. Cravens, Diurnal and seasonal effects in *E* region low-latitude nitric oxide, *J. Geophys. Res., 83,* 2453–2456, 1978.

Stolarski, R. S., and R. J. Cicerone, Stratospheric chlorine: A possible sink for ozone, *Can. J. Chem., 52,* 1610–1620, 1974.

Swider, W., The determination of the optical depth at large solar zenith angles, *Planet. Space Sci., 12,* 761–782, 1964.

Thompson, B. A., P. Harteck, and R. R. Reeves, Ultraviolet absorption coefficients of CO_2, CO, O_2, H_2O_2, N_2O, NH_3, NO, SO_2, and CH_4 between 1850 and 4000Å, *J. Geophys. Res., 68,* 6431, 1963.

U.S. Standard Atmosphere Supplements, Washington, D. C., 1966.

Vernazza, J. E., E. H. Avrett, and R. Loeser, Structure of the solar chromosphere, 2, The underlying photosphere and temperature minimum region, *Astrophys. J. Suppl. Ser., 30,* 1, 1976.

Wasser, B., and T. M. Donahue, Atomic oxygen between 80 and 120 km: Evidence for a latitudinal variation in vertical transport near the mesopause, *J. Geophys. Res., 84,* 1297–1309, 1979.

Watanabe, T., and T. Tohmatsu, An observational evidence for the seasonal variation of ozone concentrations in the upper stratosphere and mesosphere, *Rep. Ion. Space Res. Japan, 30,* 47, 1976.

Watanabe, K., M. Zelikoff, E. C. Y. Inn, Absorption coefficients of several atmospheric gases, *AFCRL Tech. Rep. 53-23,* U.S. Air Force Cambridge Res. Lab., Bedford, Mass., 1953.

Wofsy, S. C., Temporal and latitudinal variations of stratospheric trace gases: A critical comparison between theory and experiment, *J. Geophys. Res., 83,* 364–378, 1978.

Wofsy, S. C., and M. B. McElroy, HO_x, NO_x and ClO_x: Their role in atmospheric photochemistry, *Can. J. Chem., 52,* 1582–1591, 1974.

Wright, D. U., A. J. Krueger, and G. M. Foster, Rocket ozone sounding network data, *NASA TM-69365,* 1978.

(Received July 14, 1980;
revised October 9, 1980;
accepted October 19, 1980.)